

Collective excitations in chiral spin liquid: chiral roton and long-wavelength nematic mode

Hongyu Lu,^{1,2,3} Wei Zhu,⁴ and Wang Yao^{1,2,3}

¹*New Cornerstone Science Lab, Department of Physics, The University of Hong Kong, Hong Kong, China*

²*HK Institute of Quantum Science & Technology, The University of Hong Kong, Hong Kong, China*

³*State Key Laboratory of Optical Quantum Materials, The University of Hong Kong, Hong Kong, China*

⁴*Department of Physics, School of Science, Westlake University, Hangzhou 310030, China*

(Dated: January 29, 2026)

Chiral spin liquid (CSL) is a magnetic analogue of the fractional quantum Hall (FQH) liquid. Collective excitations play a vital role in shaping our understanding of these exotic quantum phases of matter and their quantum phase transitions. While the magneto-roton and long-wavelength chiral graviton modes in the FQH liquids have been extensively explored, the collective excitations of CSLs remain elusive. Here we explore the collective excitations in the SU(2) symmetric CSL phase of the spin-1/2 square-lattice $J_1 - J_2 - J_\chi$ model, where an intriguing quantum phase diagram was recently revealed. Combining exact diagonalization and time-dependent variational principle calculations, we observe two spin-singlet collective modes: a chiral p-wave (low-energy) roton mode at finite momentum and a d-wave (higher-energy) nematic mode at zero momentum, both of which are prominent across the CSL phase. Such exotic modes exhibit fingerprints distinct from those of FQH liquids, and to the best of our knowledge, are reported for the first time. By tuning J_2 , we find the nematic mode to be pronouncedly soft, together with the spin-triplet two-spinon bound states, potentially promoting strong nematic and spin stripe instabilities. Our work paves the way for further understanding CSL from the dynamical perspective and provides new spectroscopic signatures for future experiments of CSL candidates.

Introduction.— Quantum spin liquid (QSL) is a central theme in strongly correlated systems, with long-range entanglement, emergent gauge fields, and fractionalized excitations [1–3]. One particularly striking class is the chiral spin liquids (CSLs) that break time-reversal symmetry (TRS) and realize topological order [4, 5], providing a close magnetic analogue of fractional quantum Hall (FQH) liquids [6–8]. The topological nature and ground-state (GS) properties of such CSLs are well established [9–14]. However, the dynamical properties, especially the bulk collective excitations, still remain elusive, even for the simplest Kalmeyer–Laughlin (KL) CSL (magnetic realization of the bosonic 1/2 Laughlin state [15]), despite the understanding of fractionalized spinons [16]. This is an essential and fundamental question and would also provide insights to future experimental probes of such long-sought CSLs.

In FQH systems, the prototypical example of a neutral collective excitation is the magneto-roton mode, normally with energy minima at finite wave vectors [17–19]. In the long-wavelength limit, a distinct collective mode emerges at higher energy: a chiral and quadrupolar orbital spin-2 excitation, also known as the chiral graviton mode [20–22]. These modes have been numerically identified [23–26] and experimentally detected in two-dimensional electron gas [27, 28]. And their nature in fractional Chern insulators (FCIs) – the zero-field lattice-based cousins of FQH states – has also spurred intensive theoretical investigations [29–35]. CSLs share profound similarities with FQH liquids in their ground-state topology. Yet, it remains unexplored whether — and in what form — their collective excitations exhibit analogous phenomenology, particularly in SU(2)-invariant quantum magnets.

Here, we address these open questions by systematically investigating the collective excitations of a SU(2) symmetric CSL. Intriguingly, we discover a chiral p-wave roton mode and a d-wave nematic mode in the spin-singlet sector [Fig. 1(b)], both of which are distinct from the known

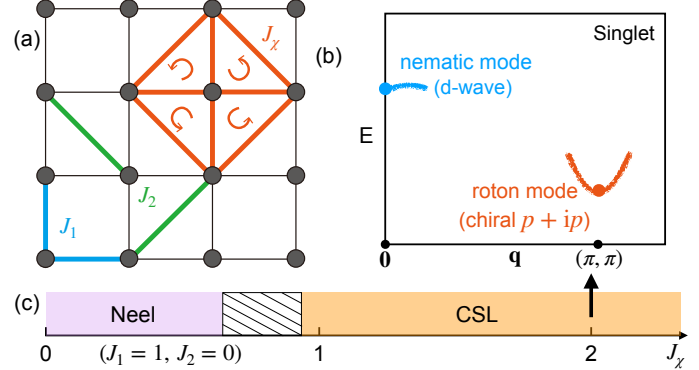


FIG. 1. Lattice model and phase diagram. (a) The $J_1 - J_2 - J_\chi$ model on square lattice. (b) Schematic plot of the two exotic spin-singlet collective modes deep inside the CSL phase. For positive J_χ the chiral roton mode lies in the $p + ip$ channel. (c) The quantum phase diagram with fixed $J_1 = 1$, $J_2 = 0$ and tuning J_χ . The GS in the shaded region is still under debate and is not the focus of this work.

knowledge of the FQH liquid. These exotic collective modes are directly revealed, combining exact diagonalization (ED), density matrix renormalization group (DMRG), and time-dependent variational principle (TDVP) calculations on the spin-1/2 $J_1 - J_2 - J_\chi$ model on square lattice. The p-wave roton is the lowest energy mode, found at $\mathbf{q} = (\pi, \pi)$, with chirality locked to the GS chirality, and it remains prominent even near the phase boundaries. The higher-energy d-wave mode at $\mathbf{q} = 0$ can be pronouncedly softened at finite J_2 , indicating the nematic instability. In addition, the spin-triplet collective excitations are also studied, with some finite-momentum two-spinon bound states observed. These findings offer insights into the dynamical landscape of CSL, thereby prompting a fundamental question concerning the nature of CSL: how dif-

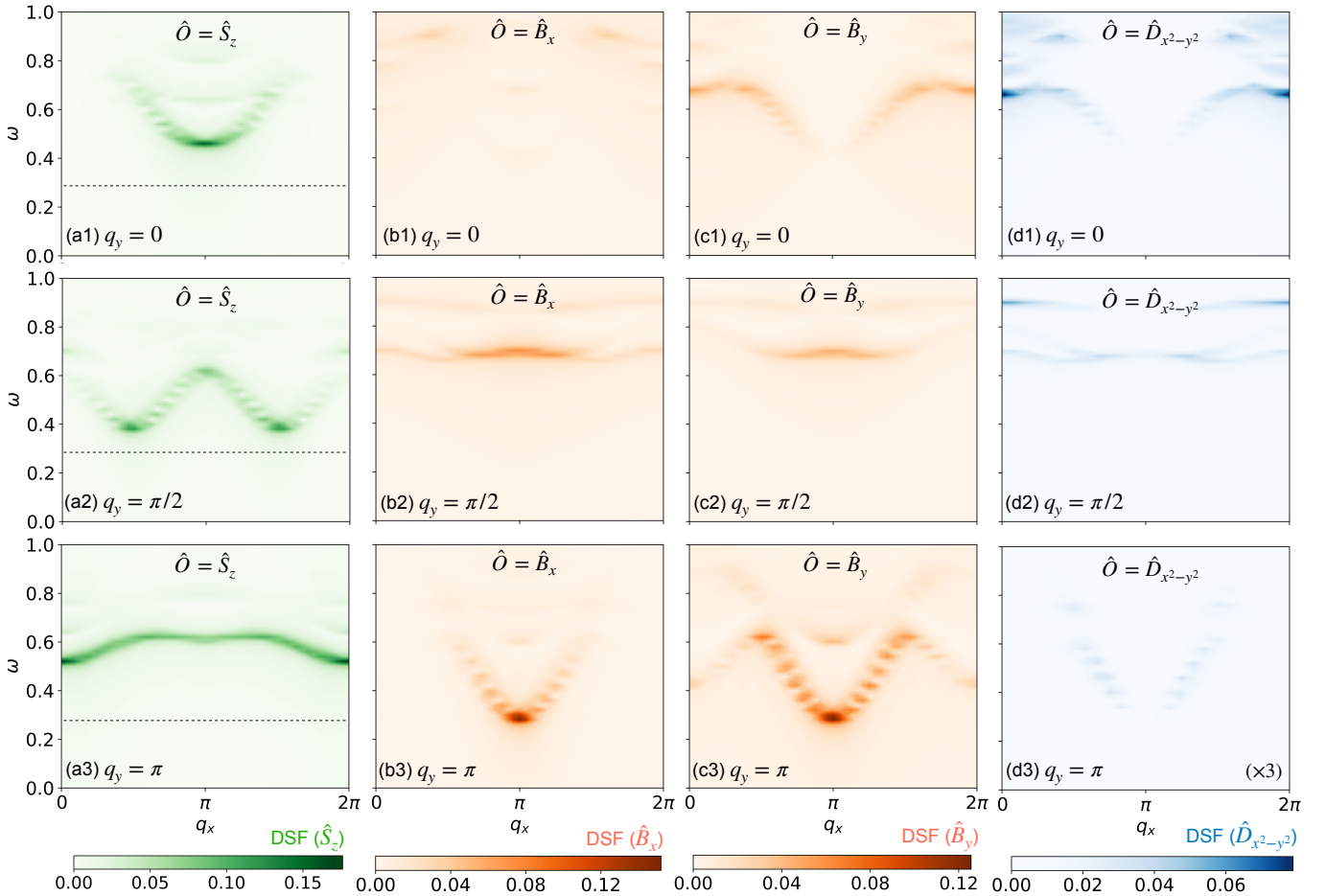


FIG. 2. Dynamical structure factors of CSL. Different panels show dynamical response of (a1-a3) spin S_z , (b1-b3) x-direction bond operator B_x , (c1-c3) y-direction bond operator B_y and (d) d-wave bond operator D (details see main text). The calculations are performed by the TDVP for $J_2 = 0$ and $J_\chi = 2$ on $L_y \times L_x = 4 \times 32$ cylinders. The horizontal/vertical axis is the energy/ q_x in each panel with different fixed q_y . The dashed lines in (a1-a3) correspond to the energy scale of the singlet roton mode ($\omega \sim 0.28$). In (d3), the DSF along $q_y = \pi$ are multiplied by a factor of three for visibility.

ferent is CSL from the established FQH/FCI paradigm despite their ground states are topologically equivalent?

Dynamical structure factors of the CSL.— To investigate the collective excitations of the CSL, we probe the dynamical responses of the CSL living in a spin-1/2 Heisenberg model on the square lattice [36–39]. The model reads

$$\hat{H} = J_1 \sum_{\langle i,j \rangle} \hat{\mathbf{S}}_i \cdot \hat{\mathbf{S}}_j + J_2 \sum_{\langle\langle i,j \rangle\rangle} \hat{\mathbf{S}}_i \cdot \hat{\mathbf{S}}_j + J_\chi \sum_{\triangle} \hat{\mathbf{S}}_i \cdot (\hat{\mathbf{S}}_j \times \hat{\mathbf{S}}_k),$$

where J_1 (fixed $J_1 = 1$ as the energy scale throughout this work) and J_2 are the nearest-neighbor (NN) and next-NN antiferromagnetic (AFM) Heisenberg interactions. J_χ refers to the three-spin scalar chiral coupling, with \triangle including four kinds of minimal triangles in each plaquette, and i, j, k follow the counterclockwise order, as shown in Fig. 1(a). The GS phase diagram of tuning J_χ with fixed $J_2 = 0$ has been studied [37, 38], as illustrated in Fig. 1(c), where a robust CSL phase exists driven by a finite J_χ . While the existing studies [37, 38] focus on the static ground state properties, the dy-

namical features of the CSL has never been studied before.

We probe the dynamical structure factors (DSFs) for several local observables:

$$\text{DSF}^{\hat{O}}(\mathbf{q}, \omega) = \sum_{\mathbf{r}, t} \frac{e^{i\omega t - \eta t} e^{-i\mathbf{q}\mathbf{r}}}{\sqrt{N_t}} (\langle \hat{O}_\mathbf{r}^\dagger(t) \hat{O}_\mathbf{0}(0) \rangle - \langle \hat{O}_\mathbf{r}^\dagger \rangle \langle \hat{O}_\mathbf{0} \rangle), \quad (2)$$

where \mathbf{q} and ω denotes the crystal momentum and frequency. The time-dependent quantity is $\hat{O}_\mathbf{r}(t) = e^{i\hat{H}t} \hat{O}_\mathbf{r} e^{-i\hat{H}t}$, and \hat{O} is the local operator. The results of DSFs (at $J_2 = 0$, $J_\chi = 2$ for example) are shown in Fig. 2.

First, we begin with the triplet sector, as is customary in the study of spin liquids, and present the spin DSFs by targeting $\hat{O} = S^z$ operator in Fig. 2(a1-a3), where the full dispersion along q_x is resolved at several relevant q_y . Rather than a purely featureless continuum, we find some finite-momentum bound states with relatively concentrated spectral weight. One notable feature is that these modes appear in relatively high-frequency regime.

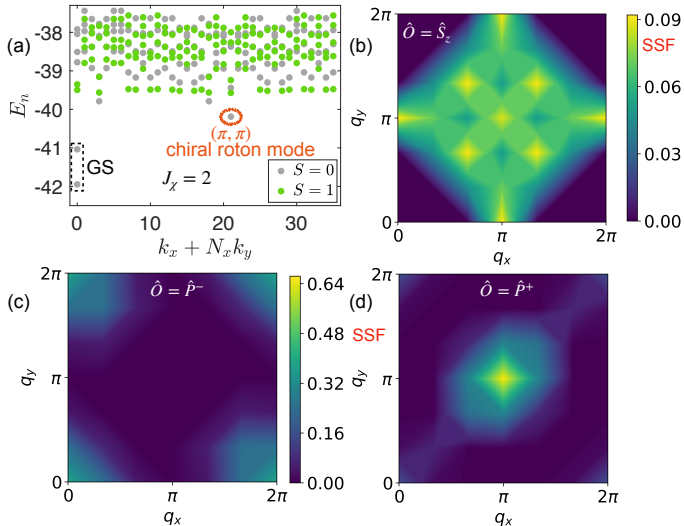


FIG. 3. **Spectral property of CSL.** (a) Low-energy spectrum obtained on a 6×6 torus by setting $J_2 = 0$, $J_x = 2$. A roton mode appears at (π, π) . The states of larger S are at higher energies. The static structure factors (SSFs) of B_x , B_y operator are shown in (b-d) with panels (c) and (d) sharing the same color bar.

Second, for the singlet sector, we naturally study the bond operators: $\hat{B}_\mu(\mathbf{r}) = \hat{\mathbf{S}}_\mathbf{r} \cdot \hat{\mathbf{S}}_{\mathbf{r}+\mu}$ ($\mu \in \{\mathbf{x}, \mathbf{y}\}$ are the primitive vectors along two directions), as they are the simplest ones that conserve the total spin. The spectra of $\hat{O} = \hat{B}_x$ and \hat{B}_y are shown in Fig. 2(b1-b3,c1-c3), respectively. Interestingly, we observe a pronounced roton mode with the energy minimum at (π, π) where the spectral weight peaks. Importantly, in a large region of the CSL parameter space [40], this $S = 0$ roton mode at (π, π) remains the lowest excitation, much lower than the spin triplet excitations.

Furthermore, in the DSFs of \hat{B}_y operator here, we also observe some non-vanishing signals at $\mathbf{q} \rightarrow 0$, which are much weaker than the roton minimum and at higher energies (the signal of \hat{B}_x is weaker possibly due to the cylinder geometry [40]). This differs from the FQH/FCI systems [18, 26], where the magneto-roton mode comes from the single-mode approximation (SMA) using the (projected) density operator. That description could become ineffective in the long-wavelength limit (even without projection), as the density operator at $\mathbf{q} = 0$ refers to the conserved total density. Instead the long-wavelength graviton mode in FQH systems is captured by the q^2 term in the small- q expansion of the projected density operator [41]. In contrast, the bond operators of the CSL are fundamentally different as they do not correspond to any conserved quantity at $\mathbf{q} = 0$.

Third, inspired by the orbital spin-2 nature of the graviton mode in FQH systems, we explore if the $\mathbf{q} = 0$ signal here is related to any orbital spin-2 excitation [21, 24, 28, 41]. Therefore, we define the d-wave operator $\hat{D}_{x^2-y^2} \equiv \hat{B}_x - \hat{B}_y$, and the DSFs are shown in Fig. 2(d1-d3). In this rank-2 quadrupolar channel, the $\mathbf{q} = 0$ signal indeed manifests as a pronounced spectral peak. We refer to this higher energy

Overlaps	$\langle \psi_0(\pi, \pi) \hat{O} \tilde{\psi}_0(0, 0) \rangle$	$ \langle \psi_0(\pi, \pi) \hat{O} \tilde{\psi}_0(0, 0) \rangle $		
Size: \hat{O}	\hat{B}_x	\hat{B}_y	$\hat{B}_x + i\hat{B}_y$	$\hat{B}_x - i\hat{B}_y$
$L_y \times L_x$				
4×4	$0.71 + 0.48i$	$0.48 - 0.71i$	0.96	0.00
4×6	$-0.13 + 0.84i$	$0.80 + 0.12i$	0.93	0.06

TABLE I. **Chiral nature of the roton mode.** The wave function overlap using the SMA reveals the lowest excited state $|\psi_0(\mathbf{k} = (\pi, \pi))\rangle$ is chiral. The wave function overlap $\langle \psi_0(\pi, \pi) | \hat{O} | \tilde{\psi}_0(0, 0) \rangle$ is properly normalized by imposing $\langle \tilde{\psi}_0(0, 0) | \hat{O}^\dagger \hat{O} | \tilde{\psi}_0(0, 0) \rangle = 1$, i.e., the excited state $\hat{O} | \tilde{\psi}_0(0, 0) \rangle$ is renormalized to unit norm.

mode at long-wavelength limit as the nematic mode. Notably, it can soften upon tuning parameters, making it more accessible, and we will discuss more later. At finite momentum, the DSF spectral response in the d-wave channel is rather weak and fades away when approaching the roton mode.

Nature of the chiral roton.— To provide further insight on the observed roton mode, we show the energy spectrum of the CSL on torus in Fig. 3. We find that the lowest excitation belongs to the spin singlet and is located at (π, π) . Its quantum number matches that of the roton mode we found in Fig. 2(b-c). The precise nature of this low-energy excitation can be obtained by inspecting its content using the SMA. As shown in Tab. I, on the symmetric torus, we find very high overlaps between the target excited state and the variational states made of \hat{B}_x and \hat{B}_y [42]. More interestingly, we find the relation $\hat{B}_x | \tilde{\psi}_0(0, 0) \rangle = i\hat{B}_y | \tilde{\psi}_0(0, 0) \rangle$ exactly holds. This motivates us to design the chiral p-wave operators $\hat{P}^\pm = \hat{B}_x \pm i\hat{B}_y$. The overlap of the new chiral states is either close to 1 (larger than the \hat{B}_μ operators) or 0, and we have checked that the chirality is locked to the GS chirality, which could be simply flipped by the sign of J_x . We have also checked that the chirality of this excited state is well retained even for the non-symmetric torus such as the 4×6 one [Tab. I], and the aforementioned properties are consistently found across the CSL phase [40].

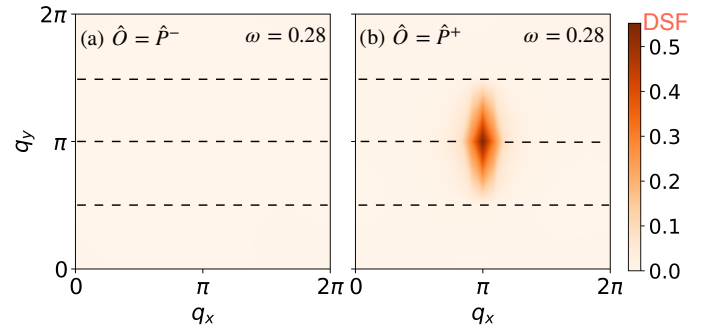


FIG. 4. **The chiral roton.** DSFs of the chiral p-wave operators \hat{P}^\pm at fixed $\omega = 0.28$ (energy scale of the roton mode) for $J_2 = 0$ and $J_x = 2$ are shown, respectively. The calculations are performed by the TDVP on $L_y \times L_x = 4 \times 32$ cylinders. The black dashed lines denote $q_y = \frac{\pi}{2}, \pi, \frac{3\pi}{2}$, respectively.

Furthermore, we test the SMA picture by computing the

static structure factors (SSFs). For the \hat{P}^+ channel, there is a peak at (π, π) , which is stronger than those of the \hat{B}_μ operators even after renormalization [40], implying the larger frequency-integrated dynamical spectral weight in this chiral channel. Interestingly, for the \hat{P}^- channel, the SSF at (π, π) is ~ 0 . These results further support that the low-energy state at (π, π) we observe is consistent with a chiral p-wave mode, which we call the chiral roton mode. To further confirm this chiral p-wave roton mode, we show the DSFs of the \hat{P}^\pm channels at fixed $\omega = 0.28$ (the energy of the roton mode) from TDVP simulations in Fig. 4. The full dispersion is included in the SI [40]. We observe a sharp peak at (π, π) in the \hat{P}^+ channel, while there is no response in the \hat{P}^- one. These are consistent with the earlier ED results in Fig. 3 and Tab. I, and together support the chiral p-wave nature of the observed singlet roton mode. This unexpected discovery distinguishes this CSL from the Laughlin FQH states whose magnetoroton modes at the finite-wave-vector minima do not carry any independent chirality quantum number, since it is created in the scalar density channel, despite the GS chirality [18, 25].

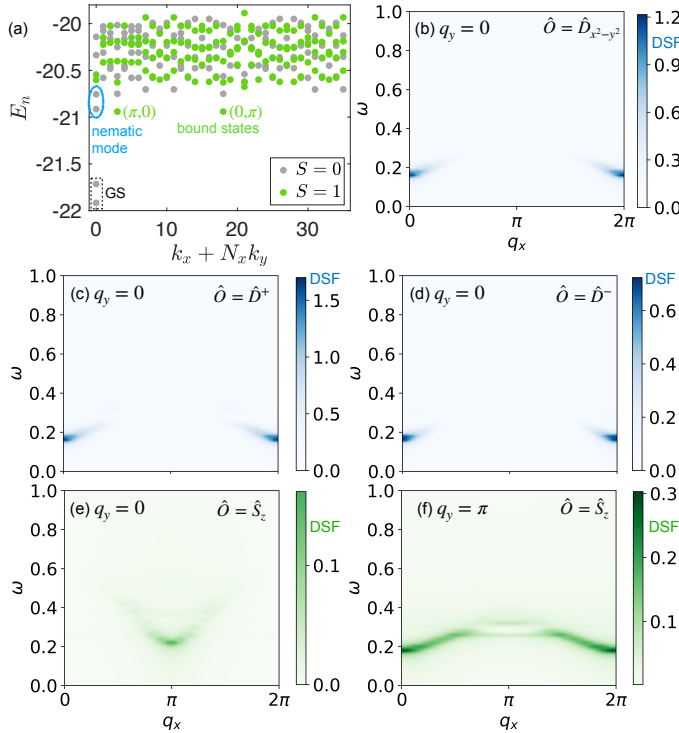


FIG. 5. **Soft collective modes.** (a) The energy spectrum of $J_2 = 0.6, J_x = 0.5$ on the 6×6 torus. The TDVP results of different channels on the 4×32 cylinders are shown in panels (b-f). The horizontal/vertical axis is the energy/ q_x in each panel with different fixed q_y .

Nature of the long-wavelength nematic mode.— Next we shift our focus to the lowest excitation mode in $\mathbf{q} = 0$ sector. We find this mode would become soft by increasing a competing J_2 interaction. We use $J_2 = 0.6$, and $J_x = 0.5$ as an example and show the energy spectrum on the 6×6 torus in Fig. 5 (a). Notably, in the singlet subspace, the lowest excited states are

$ \tilde{\psi}\rangle$	$ \tilde{\psi}_0(0,0)\rangle$			$ \tilde{\psi}_1(0,0)\rangle$		
$\langle \tilde{\psi} \hat{O} \tilde{\psi} \rangle$	$\hat{D}_{x^2-y^2}$	\hat{D}^+	\hat{D}^-	$\hat{D}_{x^2-y^2}$	\hat{D}^+	\hat{D}^-
$ \langle \tilde{\psi}_2(0,0) $	0.811	0.735	0.722	0.000	0.000	0.000
$ \langle \tilde{\psi}_3(0,0) $	0.000	0.000	0.000	0.809	0.716	0.736

TABLE II. **Overlap of the nematic mode.** We show the absolute values of the overlaps ($|\langle \tilde{\psi} | \hat{O} | \tilde{\psi} \rangle|$) from the ED results for different d-wave operators at $J_2 = 0.6, J_x = 0.5$ on the 6×6 torus. $|\tilde{\psi}_{0,1}(0,0)\rangle$ are the two lowest states in the $(0,0)$ momentum sector (the 2-fold degenerate GSs of the CSL) after normalization by imposing $\langle \tilde{\psi}_{0,1}(0,0) | \hat{O}^\dagger \hat{O} | \tilde{\psi}_{0,1}(0,0) \rangle = 1$, i.e., the excited state $\hat{O} | \tilde{\psi}_{0,1}(0,0) \rangle$ is renormalized to unit norm. $|\langle \tilde{\psi}_{2,3}(0,0) |$ are the two lowest excited states above the two GSs in the $(0,0)$ momentum sector.

now in the zero-momentum sector, in contrast to the spectra deep in the CSL phase (c.f. Fig. 3 (a)), where a higher-energy nematic mode has been found at $\mathbf{q} = 0$. This motivates us to explore the relation between these low-energy states here and the previously studied nematic mode. The overlaps between the approximated nematic mode and the low-energy excited states based on the ED results are shown in Tab. II. Apart from using the $\hat{D}_{x^2-y^2}$ operator to check the orbital spin-2 characteristic, we also try to explore its chirality motivated by the fact that the graviton mode in the FQH system is chiral [24]. Therefore, we further design the chiral operators: $\hat{D}^\pm = \hat{D}_{x^2-y^2} \pm i\hat{D}_{xy}$, where $\hat{D}_{xy} = \hat{B}_{x,y} - \hat{B}_{-x,y}$ is composed of the next-NN bonds.

Interestingly, we find that the $\hat{D}_{x^2-y^2}$ operator exhibits a one-to-one (diagonal) selection rule between the two degenerate GSs and the two lowest excited states (circled in blue in Fig. 5(a)) with very high overlaps, supporting that these excitations are well captured by a single-mode ansatz. In addition, according to the overlaps of the \hat{D}^\pm channels, no obvious chirality is observed. We further show the DSFs of different d-wave operators with fixed $q_y = 0$ on the 4×32 cylinder in Fig. 5 (b-d) [40]. It is consistent with the ED results that the nematic mode (at higher energy at parameters deep in the CSL phase) becomes pronouncedly soft, and the DSF of the nematic mode is significantly sharp with highly concentrated spectral weight, exhibiting strong nematic instability. Although the different chiral d-wave operators show different absorption strengths, they are of the same order of magnitude, and the peak positions remain essentially unchanged.

Spin triplet excitations.— For the triplet sector deep in the CSL phase ($J_2 = 0, J_x = 2$), we also show the spin SSF (using \hat{S}_z for example) in Fig. 3(b). Although no obvious feature can be directly captured from the continuum of the spectrum in Fig. 3 (a), there are some relative peaks in the SSFs at finite momentum, which are consistent with the possible bound states observed from the DSFs in Fig. 2(a1-a3). Note that, in contrast to those of bond operators, there is vanishing weight at $\mathbf{q} \rightarrow 0$ as the total spin is conserved.

The DSFs of the spin excitations are also studied at $J_2 = 0.6$ and $J_x = 0.5$ [5(e-f)] and we observe the $(\pi, 0)/(0, \pi)$

triplet mode at the energy minimum (the spectral weight is relatively smaller at $(\pi, 0)$ due to the cylinder geometry). The energy gap of the triplet mode and that of the nematic mode are very close and this is consistent with the ED spectrum in Fig.5(a). This triplet mode is consistent with a two-spinon bound state characterized by pronounced spin stripe fluctuations. Further, this triplet mode is closely connected to the nematic mode [38], since it also carries nematic fluctuations.

Discussions and implications.— In this work, we have presented a systematic study of the collective excitations of CSL. Although the topological order of many-body ground states is the same as the 1/2 Laughlin FQH/FCI states, we find their low-lying collective excitations are quite different. In the singlet sector, we observe a prominent low-energy chiral p-wave roton mode at finite momentum, which is prominent throughout the phase parameter space. By contrast, in the FQH/FCI systems, the roton minimum of the magnetoroton mode exhibits no chirality or orbital spin [18]. This is an unexpected result and is reported for the first time, to the best of our knowledge. Furthermore, we have also observed a $\mathbf{q} = 0$ d-wave nematic mode, which is similar to the chiral graviton mode in FQH/FCI systems in the aspect of the orbital spin-2 and the fact that it is at higher energy when far from the phase boundaries [24]. However, we observe no obvious chirality of the nematic mode in the CSL. Although the chiral roton mode and the nematic mode exhibit different characteristics, the dispersions suggest that they may be connected. Whether they belong to the same excitation branch is interesting for further studies.

Our findings underscore the significance of investigating the collective excitations in the CSLs, since these systems are often assumed to exhibit only a continuum. The collective modes could be intrinsic to such topological liquids and might play a role comparable to that of the magnetoroton and graviton modes in shaping our understanding of FQH liquids [18, 43]. This could also motivate further investigations of collective modes in other CSLs (such as non-abelian ones) and different QSLs (with different or without topological orders). Since the model in this work is based on the square lattice with C_4 symmetry, it would be interesting for future work to explore how the lattice geometries and symmetries could affect the collective modes discovered in this work. Note that, this could be very different from the Laughlin FCIs with different discrete rotation symmetries, where the magnetoroton minima are consistently found without orbital spin or chirality, and the spin-2 gravitons are consistently found to be chiral [29, 31–33, 35].

Experimentally, detecting a CSL is often more demanding than detecting a fermionic FQH/FCI phase. In FQH/FCI systems, topological order is accompanied by quantized charge transport responses [6], while in CSLs the corresponding signatures are carried by neutral spin/energy currents and are typically accessed only indirectly [8, 44]. Therefore, additional experimental probes are highly desirable, and one promising route is to detect the dynamical properties and excitations. Inelastic neutron scattering is the primary momentum-resolved

probe of spin excitations, and it predominantly accesses the $S = 1$ channel in an SU(2)-symmetric system with a singlet ground state [3]. However, a broad continuum and even the bound-state-like features in the triplet channel are insufficient for identification. In this work, the singlet collective modes offer new spectroscopic signatures for future experiments on candidate CSL materials. For example, the $\mathbf{q} = 0$ nematic mode could be identified from the (circularly) polarized Raman scattering measurements [28, 45, 46], where symmetry selection rules allow one to isolate the d-wave channel (B_{1g} channel for this model) [47], and it is also interesting to experimentally explore whether the nematic mode is chiral. A possible route to access the finite- \mathbf{q} chiral p-wave roton mode is momentum- and polarization-resolved (indirect) resonant inelastic X-ray scattering measurements [48, 49], where circular-polarization dependence might provide a direct way to distinguish \hat{P}^\pm channels through chiral selection rules.

We close by highlighting the soft collective modes in the CSL are related to interesting quantum phase transitions. For example, we study the soft modes at $J_2 = 0.6$ and $J_\chi = 0.5$, but the GS phase diagram at fixed $J_\chi = 0.5$ larger J_2 is still under debate. Ref. [37] suggests a direct CSL-stripe transition at $J_2 \sim 0.75$ based on DMRG results and the spin stripe order is $(0, \pi)$ or $(\pi, 0)$. However, Ref. [38] suggests the possibility of an intermediate nematic spin liquid phase between the CSL and stripe phases, based on the 32-site ED results, but the identification of the nematic phase still suffers from the finite-size effect. In fact, the soft collective modes reported in our work are consistent with both scenarios. For the first one, if the CSL-stripe transition is continuous, one might observe the $\mathbf{q} = 0$ nematic mode and $(0, \pi)/(\pi, 0)$ triplet mode both become gapless at the critical point, and the stripe phase itself has the co-existing secondary nematic order. For the second scenario, the nematic spin liquid phase shall be a nematic CSL, and the two-step transition could be triggered by the sequential gap closing of the nematic and triplet modes in the CSL. This two-step transition also leads to a unique vestigial scenario [50–52], in which the vestigial nematic phase inherited from stripe order is topologically ordered. The mechanism for the nematic CSL discussed here echoes that of FQH nematics [53–55] and smectic FCIs [56, 57], where the latter phases are triggered by the soft chiral graviton at $\mathbf{q} = 0$ and magneto-roton at finite momentum, respectively, and the topological orders remain intact through the symmetry-breaking process. A more extensive exploration of the parameter space is required, and either interesting scenario may be realized in a broader regime, which we leave for future work.

METHODS

The low-energy excitations of the CSL in the model Hamiltonian Eq. (1) are numerically simulated using the exact diagonalization (ED) [58], density matrix renormalization group (DMRG) [59], and time-dependent variational principle (TDVP) methods [60].

Energy spectra

The energy spectra are calculated by the ED. For the ED simulations, we use the Lanczos algorithm, working in symmetry-resolved sectors that exploit translation (crystal momentum) and total S_z conservation [58]. Part of the ED simulations are carried out using QuSpin package [61]. The system size in the ED calculation varies from $N_s = 16$ to 36. The Hilbert subspace of the $N_s = 36$ in each momentum sector has $\sim 2.52 \times 10^8$ basis states, which is close to the practical computational limit of our ED calculations.

Within the single-mode approximation (SMA), the low-energy excitation could be constructed by applying the local operator to the many-body ground state: $|\psi(\mathbf{q})\rangle = O(\mathbf{q})|\psi_0(\mathbf{q} = (0, 0))\rangle$. The comparison of this SMA-inspired state with the ED calculation may validate the operator content of the low-energy excited state.

Dynamical Structure Factors

The dynamical response can be accessed by the tensor network simulations. We perform finite and infinite DMRG simulations [59] with global S_z -conservation implemented. To calculate DSFs (see Eq. 2), we compute the time-dependent correlation function using the TDVP simulations [60]:

$$\langle 0 | \hat{O}_r^\dagger(t) \hat{O}_0 | 0 \rangle = e^{iE_0 t} \langle 0 | \hat{O}_r e^{-i\hat{H}t} \hat{O}_0 | 0 \rangle, \quad (3)$$

where $|0\rangle$ is the ground-state wavefunction. To obtain the DSF of each local operator \hat{O} , in practice, we evolve the state $\psi(t) = e^{-i\hat{H}t} \hat{O}_0 |0\rangle$ step by step with $\Delta t = 0.05$, and the correlator is measured after each time step. For the results in the main text, we evolve totally $N_t = 1000$ steps such that the TDVP spectra are obtained on a frequency grid with spacing $\Delta\omega = 0.02$. In the time-to-frequency Fourier transform, we have used the Lorentzian broadening $\eta = 0.05$. The bond dimension for the TDVP results is up to $\chi = 400$, which provides well converged results for the studied systems in this work [40]. TeNPy library is used in these matrix-product-state simulations [62].

As a byproduct, the static structure factor (SSF) can be calculated using the equal-time correlators $\sum_r e^{-i\mathbf{q} \cdot \mathbf{r}} (\langle \hat{O}_0^\dagger \hat{O}_r \rangle - \langle \hat{O}_0^\dagger \rangle \langle \hat{O}_r \rangle)$. The Fourier transformation leads to the SSF defined in the momentum space.

Author contributions

H.L. initiated the project and performed the numerical simulations. All authors contributed to the discussion, analysis of the data and writing of the manuscript.

Data availability

The data supporting the plots within this paper and other findings of this study are available from the corresponding author upon reasonable request.

Acknowledgments

H. L. thanks Jie Wang and Xin Shen for helpful discussions, and Xiao-Tian Zhang and Han-Qing Wu for some ground-state benchmark, and Min Long, Zeno Bacciconi, Herman B. Xavier, Zi Yang Meng, and Marcello Dalmonte for collaborations in studying the FCI excitations, and Zheng Yan for the hospitality at the early stage of this project. W. Z. thanks S. S. Gong, J. W. Yang, L. Wang for collaborating and fruitful discussion on the previous projects. H. L. and W. Y. are supported by the National Natural Science Foundation of China (No. 12425406), Research Grant Council of Hong Kong (AoE/P-701/20, HKU SRFS21227S05), and New Cornerstone Science Foundation. We thank Beijing PARATERA Tech Co., Ltd. (<https://cloud.paratera.com>) for providing HPC resources that supported the research results reported in this paper. This work is also supported by the National Key Research and Development Program of China Grant No. 2022YFA1402204.

- [1] L. Savary and L. Balents, *Reports on Progress in Physics* **80**, 016502 (2016).
- [2] Y. Zhou, K. Kanoda, and T.-K. Ng, *Rev. Mod. Phys.* **89**, 025003 (2017).
- [3] C. Broholm, R. J. Cava, S. A. Kivelson, D. G. Nocera, M. R. Norman, and T. Senthil, *Science* **367**, eaay0668 (2020), <https://www.science.org/doi/pdf/10.1126/science.aay0668>.
- [4] V. Kalmeyer and R. B. Laughlin, *Phys. Rev. Lett.* **59**, 2095 (1987).
- [5] X. G. Wen, F. Wilczek, and A. Zee, *Phys. Rev. B* **39**, 11413 (1989).
- [6] H. L. Stormer, D. C. Tsui, and A. C. Gossard, *Rev. Mod. Phys.* **71**, S298 (1999).
- [7] K. Yang, L. K. Warman, and S. M. Girvin, *Phys. Rev. Lett.* **70**, 2641 (1993).
- [8] F. D. M. Haldane and D. P. Arovas, *Phys. Rev. B* **52**, 4223 (1995).
- [9] A. E. B. Nielsen, G. Sierra, and J. I. Cirac, *Nat. Commun.* **4**, 1 (2013).
- [10] Y.-C. He, D. N. Sheng, and Y. Chen, *Phys. Rev. Lett.* **112**, 137202 (2014).
- [11] S.-S. Gong, W. Zhu, and D. N. Sheng, *Scientific Reports* **4**, 6317 (2014).
- [12] B. Bauer, L. Cincio, B. P. Keller, M. Dolfi, G. Vidal, S. Trebst, and A. W. W. Ludwig, *Nat. Commun.* **5**, 1 (2014).
- [13] A. Wietek and A. M. Läuchli, *Phys. Rev. B* **95**, 035141 (2017).
- [14] W.-J. Hu, W. Zhu, Y. Zhang, S. Gong, F. Becca, and D. N. Sheng, *Physical Review B* **91**, 10.1103/physrevb.91.041124 (2015).
- [15] R. B. Laughlin, *Phys. Rev. Lett.* **50**, 1395 (1983).
- [16] W. Zhu, S. shu Gong, and D. N. Sheng, *Proceedings of the National Academy of Sciences* **116**, 5437 (2019), <https://www.pnas.org/doi/pdf/10.1073/pnas.1807840116>.
- [17] S. M. Girvin, A. H. MacDonald, and P. M. Platzman, *Phys. Rev. Lett.* **54**, 581 (1985).
- [18] S. M. Girvin, A. H. MacDonald, and P. M. Platzman, *Phys. Rev. B* **33**, 2481 (1986).
- [19] B. Yang, *Phys. Rev. B* **87**, 245132 (2013).
- [20] F. D. M. Haldane, *Physical Review Letters* **107**, 10.1103/phys

revlett.107.116801 (2011).

[21] B. Yang, Z.-X. Hu, Z. Papić, and F. D. M. Haldane, *Phys. Rev. Lett.* **108**, 256807 (2012).

[22] S. Golkar, D. X. Nguyen, and D. T. Son, *Journal of High Energy Physics* **2016**, 10.1007/jhep01(2016)021 (2016).

[23] Z. Liu, A. Gromov, and Z. Papić, *Phys. Rev. B* **98**, 155140 (2018).

[24] S.-F. Liou, F. D. M. Haldane, K. Yang, and E. H. Rezayi, *Phys. Rev. Lett.* **123**, 146801 (2019).

[25] P. Kumar and F. D. M. Haldane, *Phys. Rev. B* **106**, 075116 (2022).

[26] Y. Liu, T. Zhao, and T. Xiang, *Phys. Rev. B* **110**, 195137 (2024).

[27] I. V. Kukushkin, J. H. Smet, V. W. Scarola, V. Uman-sky, and K. von Klitzing, *Science* **324**, 1044 (2009), <https://www.science.org/doi/pdf/10.1126/science.1171472>.

[28] J. Liang, Z. Liu, Z. Yang, Y. Huang, U. Wurstbauer, C. R. Dean, K. W. West, L. N. Pfeiffer, L. Du, and A. Pinczuk, *Nature* **628**, 78 (2024).

[29] C. Repellin, T. Neupert, Z. Papić, and N. Regnault, *Phys. Rev. B* **90**, 045114 (2014).

[30] H. Lu, B.-B. Chen, H.-Q. Wu, K. Sun, and Z. Y. Meng, *Phys. Rev. Lett.* **132**, 236502 (2024).

[31] B. M. Kousa, N. Morales-Durán, T. M. R. Wolf, E. Khalaf, and A. H. MacDonald, *Theory of magnetoroton bands in moiré materials* (2025), arXiv:2502.17574 [cond-mat.mes-hall].

[32] M. Long, H. Lu, H.-Q. Wu, and Z. Y. Meng, *Spectra of magnetoroton and chiral graviton modes of fractional chern insulator* (2025), arXiv:2501.00247 [cond-mat.str-el].

[33] Y. Wang, J. Huxford, D. X. Nguyen, G. Ji, Y. B. Kim, and B. Yang, *Dynamics and lifetime of geometric excitations in moiré systems* (2025), arXiv:2502.02640 [cond-mat.str-el].

[34] X. Shen, C. Wang, X. Hu, R. Guo, H. Yao, C. Wang, W. Duan, and Y. Xu, *Magnetorotons in moiré fractional chern insulators* (2025), arXiv:2412.01211 [cond-mat.str-el].

[35] M. Long, Z. Baccioni, H. Lu, H. B. Xavier, Z. Y. Meng, and M. Dalmonte, *Chiral graviton modes in fermionic fractional chern insulators* (2026), arXiv:2601.05196 [cond-mat.str-el].

[36] R. Samajdar, M. S. Scheurer, S. Chatterjee, H. Guo, C. Xu, and S. Sachdev, *Nature Physics* **15**, 1290 (2019).

[37] X.-T. Zhang, Y. Huang, H.-Q. Wu, D. N. Sheng, and S.-S. Gong, *Phys. Rev. B* **109**, 125146 (2024).

[38] J. Yang, Z. Liu, and L. Wang, *Phys. Rev. B* **110**, 224404 (2024).

[39] H.-K. Jin, H.-H. Tu, and Y.-H. Zhang, *Phys. Rev. B* **112**, 035159 (2025).

[40] Additional results in the Supplemental Information..

[41] B. Yang, *Phys. Rev. B* **112**, 075132 (2025).

[42] For cross-sector overlap estimates, the 6×6 cluster is not included due to the larger Hilbert-space dimension..

[43] F. D. M. Haldane, *Phys. Rev. Lett.* **107**, 116801 (2011).

[44] X.-T. Zhang, Y. H. Gao, and G. Chen, *Physics Reports* **1070**, 1 (2024), thermal Hall effects in quantum magnets.

[45] T. P. Devereaux and R. Hackl, *Rev. Mod. Phys.* **79**, 175 (2007).

[46] E. Koller, V. Leeb, N. B. Perkins, and J. Knolle, *Raman circular dichroism and quantum geometry of chiral quantum spin liquids* (2025), arXiv:2503.14091 [cond-mat.str-el].

[47] A. W. Sandvik, S. Capponi, D. Poilblanc, and E. Dagotto, *Phys. Rev. B* **57**, 8478 (1998).

[48] L. J. P. Ament, M. van Veenendaal, T. P. Devereaux, J. P. Hill, and J. van den Brink, *Rev. Mod. Phys.* **83**, 705 (2011).

[49] M. Sikora, A. Juhin, T.-C. Weng, P. Sainctavit, C. Detlefs, F. de Groot, and P. Glatzel, *Phys. Rev. Lett.* **105**, 037202 (2010).

[50] L. Nie, A. V. Maharaj, E. Fradkin, and S. A. Kivelson, *Phys. Rev. B* **96**, 085142 (2017).

[51] R. M. Fernandes, P. P. Orth, and J. Schmalian, *Annual Review of Condensed Matter Physics* **10**, 133 (2019).

[52] H. Lu, H.-Q. Wu, B.-B. Chen, and Z. Y. Meng, *Vestigial gapless boson density wave emerging between $\nu = 1/2$ fractional chern insulator and finite-momentum supersolid* (2024), arXiv:2408.07111 [cond-mat.mes-hall].

[53] N. Regnault, J. Maciejko, S. A. Kivelson, and S. L. Sondhi, *Phys. Rev. B* **96**, 035150 (2017).

[54] B. Yang, *Phys. Rev. Res.* **2**, 033362 (2020).

[55] S. Pu, A. C. Balram, J. Taylor, E. Fradkin, and Z. Papić, *Phys. Rev. Lett.* **132**, 236503 (2024).

[56] H. Lu, H.-Q. Wu, B.-B. Chen, K. Sun, and Z. Yang Meng, *Reports on Progress in Physics* **87**, 108003 (2024).

[57] H. Lu, H.-Q. Wu, B.-B. Chen, and Z. Y. Meng, *Newton* **10**.1016/j.newton.2025.100300 (2025).

[58] A. W. Sandvik, *AIP Conference Proceedings* **1297**, 135 (2010),

[59] S. R. White, *Phys. Rev. Lett.* **69**, 2863 (1992).

[60] J. Haegeman, J. I. Cirac, T. J. Osborne, I. Pižorn, H. Verschelde, and F. Verstraete, *Phys. Rev. Lett.* **107**, 070601 (2011).

[61] P. Weinberg and M. Bukov, *SciPost Phys.* **7**, 020 (2019).

[62] J. Hauschild, J. Unfried, S. Anand, B. Andrews, M. Bintz, U. Borla, S. Divic, M. Drescher, J. Geiger, M. Hefel, K. Hémery, W. Kadow, J. Kemp, N. Kirchner, V. S. Liu, G. Möller, D. Parker, M. Rader, A. Romen, S. Scalet, L. Schoonderwoerd, M. Schulz, T. Soejima, P. Thoma, Y. Wu, P. Zechmann, L. Zweng, R. S. K. Mong, M. P. Zaletel, and F. Pollmann, *SciPost Phys. Codebases* , 41 (2024).

[63] H. Li and F. D. M. Haldane, *Phys. Rev. Lett.* **101**, 010504 (2008).

[64] X.-L. Qi, H. Katsura, and A. W. W. Ludwig, *Phys. Rev. Lett.* **108**, 196402 (2012).

The supplementary information contains: I. the ground-state entanglement spectrum; II. additional ED and TDVP results of the collective modes; III. additional information of TDVP simulations.

I. GROUND-STATE ENTANGLEMENT SPECTRUM

Here, we show the entanglement spectrum from the identity sector of the CSL in Fig. S1, which is not only consistent with the edge-mode counting [63, 64] but also demonstrates the GS chirality. We note that, both the GS chirality and that of the chiral roton mode would be flipped by the sign of J_χ .

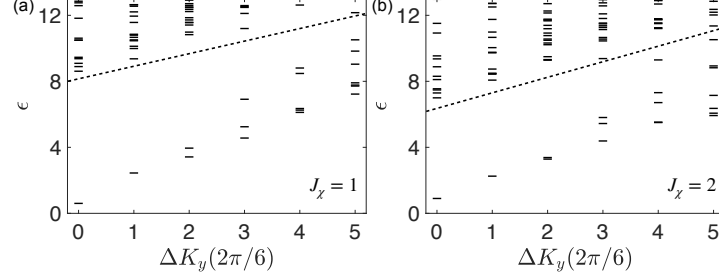


FIG. S1. **Ground-state entanglement spectrum** Here, we show the entanglement spectrum of the CSL at different parameters, demonstrating the characteristic edge-mode counting $\{1, 1, 2, 3, 5, 7, \dots\}$.

II. ADDITIONAL RESULTS OF THE COLLECTIVE MODES

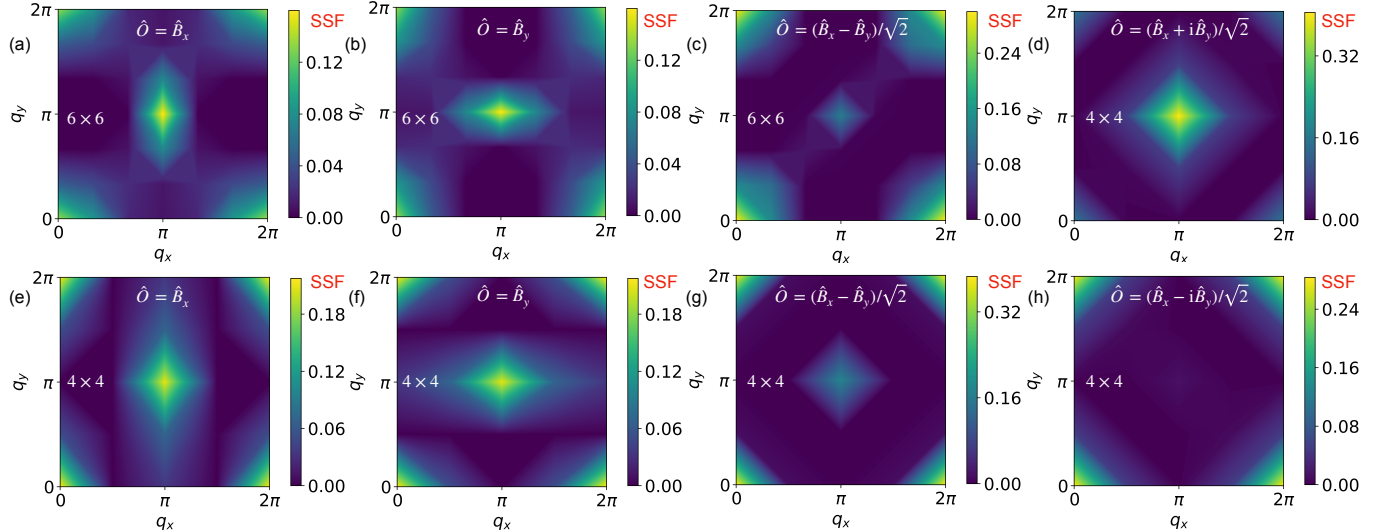


FIG. S2. **Additional results of SSFs at $J_2 = 0$, $J_\chi = 2$** . In panel (a-c), we show the complementary SSFs from the 6×6 torus. The SSFs of different channels from the 4×4 torus are shown in (d-h).

In the main text, we have shown some ED results of SSFs at $J_2 = 0$, $J_\chi = 2$ from the 6×6 torus in Fig. 3. Here, we further show the complementary SSFs in Fig. S2 (a-c). We note that the SSF peak at $\mathbf{q} = (0, 0)$ is much stronger in the d-wave channel than those of other channels. Besides, we also show the different SSFs from the 4×4 torus in Fig. S2(b-f), with similar features to those of the 6×6 torus. Further, we show the extrapolation of the d-wave SSF at $\mathbf{q} = (0, 0)$ and the chiral p-wave SSF at $\mathbf{q} = (\pi, \pi)$ in Fig. S3(a), and they both extrapolate to finite values in the thermodynamic limit. The robust nematic fluctuations from these systems with exact C_4 rotation symmetry suggest that the nematic mode reported in the main text is intrinsic in this CSL phase. In addition, the SSFs scale extensively with the system size. Accordingly, normalizing them by the number of lattice sites yields an intensive quantity, which can be used as a measure of the strength of the corresponding order parameter. The

extrapolations of the intensive quantities are shown in Fig.S3 (b). The extrapolated zeros support that the peaks in the SSFs only correspond to fluctuations and there are no symmetry-breaking orders.

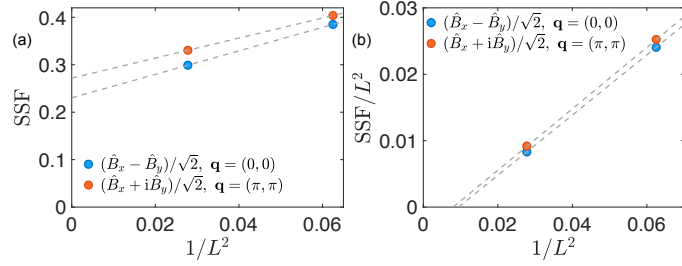


FIG. S3. **Extrapolation of SSFs at $J_2 = 0, J_\chi = 2$.** Here, we extrapolate the (a) extensive SSFs and (b) the corresponding intensive values (normalized by lattice sites) from ED simulations on symmetric tori.

For more examples, we show the ED results of the CSL phase at $J_2 = 0, J_\chi = 1.5$. In Fig.S4 (a), the low-energy spectrum from the 6×6 torus is shown, which is similar to that at $J_\chi = 1.5$ and the chiral roton mode is the lowest excitation here. We show the SSFs of different operators from the 6×6 torus as well, with similar features as reported earlier: strong d-wave nematic fluctuations at $\mathbf{q} = (0, 0)$ and chiral p-wave fluctuations at $\mathbf{q} = (\pi, \pi)$.

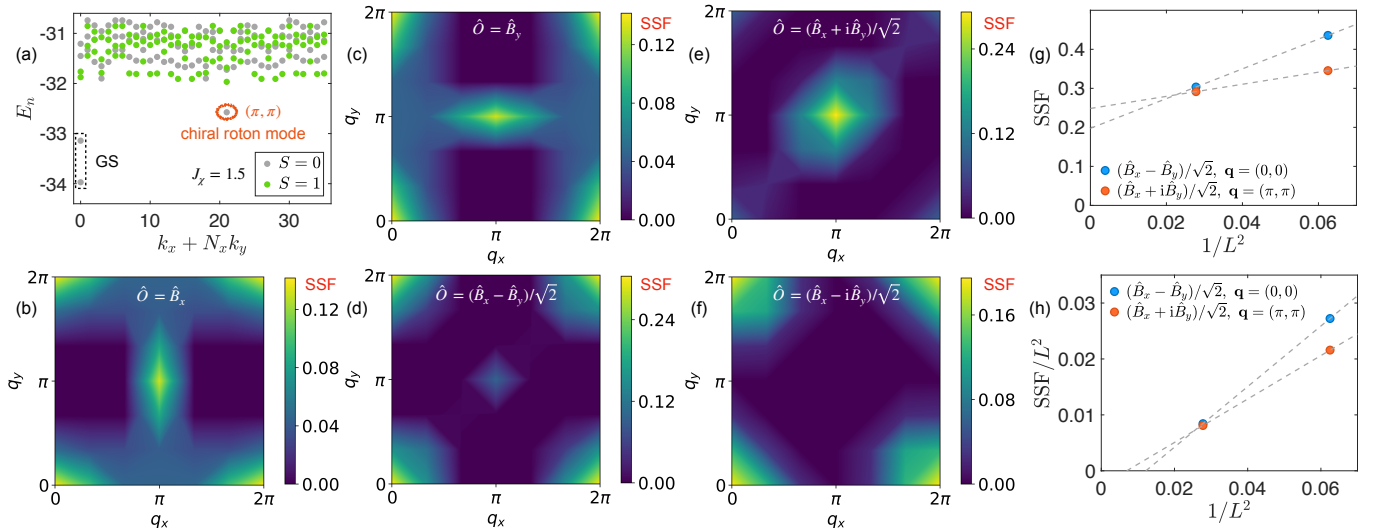


FIG. S4. **ED spectrum and SSFs at $J_2 = 0, J_\chi = 1.5$.** The ED spectrum from the 6×6 torus is shown in panel (a). The corresponding SSFs of different parameters from the 6×6 torus are shown in panels (b-f). The extrapolation of some (g) extensive SSFs and (h) the corresponding intensive values (normalized by lattice sites) from ED simulations on symmetric tori are shown.

We have also extrapolated the peaks of the SSFs as well as those normalized by the lattice sites, as shown in Fig.S4(g,h), respectively. The results are consistent with our earlier conclusions that the peaks of such SSFs are due to the intrinsic fluctuations instead of the symmetry-breaking orders.

To further substantiate the chiral roton mode, we show the overlaps between the (π, π) excited state and the corresponding trial states at different parameters (including $J_\chi = 1.5$) in Tab.S1, which further supports the chiral p-wave nature of this singlet roton mode. We note that, the chiral roton remains the lowest excitation for these considered parameters.

Overlaps	\hat{B}_x	\hat{B}_y	$\hat{B}_x + i\hat{B}_y$	$\hat{B}_x - i\hat{B}_y$
$4 \times 4, J_\chi = 1.3$	0.856	0.856	0.960	0.000
$4 \times 4, J_\chi = 1.5$	0.864	0.864	0.964	0.000
$4 \times 4, J_\chi = 1.7$	0.863	0.863	0.964	0.000
$4 \times 4, J_\chi = 1.9$	0.861	0.861	0.962	0.000
$4 \times 6, J_\chi = 1.3$	0.827	0.859	0.944	0.012
$4 \times 6, J_\chi = 1.5$	0.818	0.870	0.944	0.072
$4 \times 6, J_\chi = 1.7$	0.812	0.866	0.938	0.080
$4 \times 6, J_\chi = 1.9$	0.809	0.858	0.930	0.069

TABLE S1. **The overlaps** $\langle \psi_0(\pi, \pi) | \hat{O} | \tilde{\psi}_0(0, 0) \rangle$ **of the roton mode**. Here, $|\psi_0(\mathbf{k})\rangle$ is the lowest-energy state of the \mathbf{k} sector. $|\tilde{\psi}_0(0, 0)\rangle$ is normalized such that $\langle \tilde{\psi}_0(0, 0) | \hat{O}^\dagger \hat{O} | \tilde{\psi}_0(0, 0) \rangle = 1$. ED results with fixed $J_2 = 0$, and different J_χ, \hat{O} , and system sizes are listed.

In Fig.4 of the main text, we have shown the DSFs in the chiral p-wave channels with fixed $\omega = 0.28$ (the energy scale of the roton minimum). Here, as a complement, we show their ω -dependence in Fig.S5. The dispersion of the chiral roton is the same as that from the \hat{B}_μ operators and the spectral response fades away at other momenta.

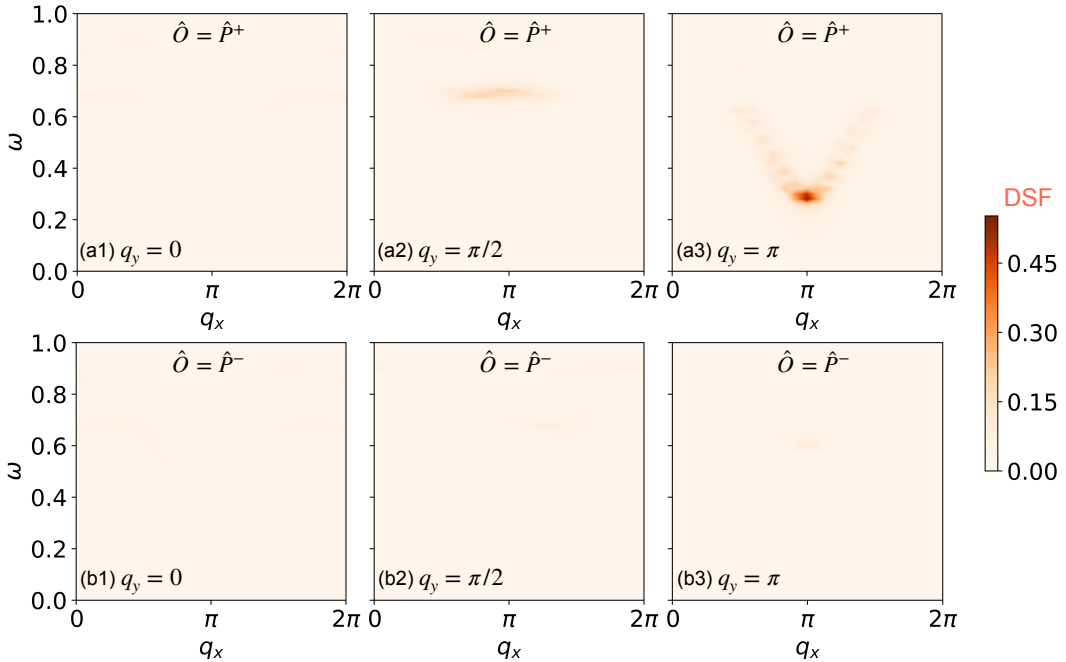


FIG. S5. **DSFs in the chiral p-wave channels.** TDVP results obtained at $J_2 = 0$ and $J_\chi = 2$. The horizontal/vertical axis is the energy/ q_x in each panel with different fixed q_y .

With strong competing J_2 , we have demonstrated that the nematic mode would be pronouncedly soft and the DSFs in the d-wave channels at $J_2 = 0.6$, $J_\chi = 0.5$ are shown in Fig.5 of the main text for example, which have vanishing response at finite \mathbf{q} . For complementary information of the singlet excitations near the phase boundaries, we further show the DSFs of the bond operators \hat{B}_μ at $J_2 = 0.6$, $J_\chi = 0.5$ in Fig.S6. While the lowest excitation is the nematic mode at $\mathbf{q} = 0$ with maximum spectral weight, the singlet excitation gap at (π, π) is still very low. More importantly, as shown in Fig.S7, the chiral p-wave roton mode with a sharp spectral peak at (π, π) is still prominent even near the phase boundaries.

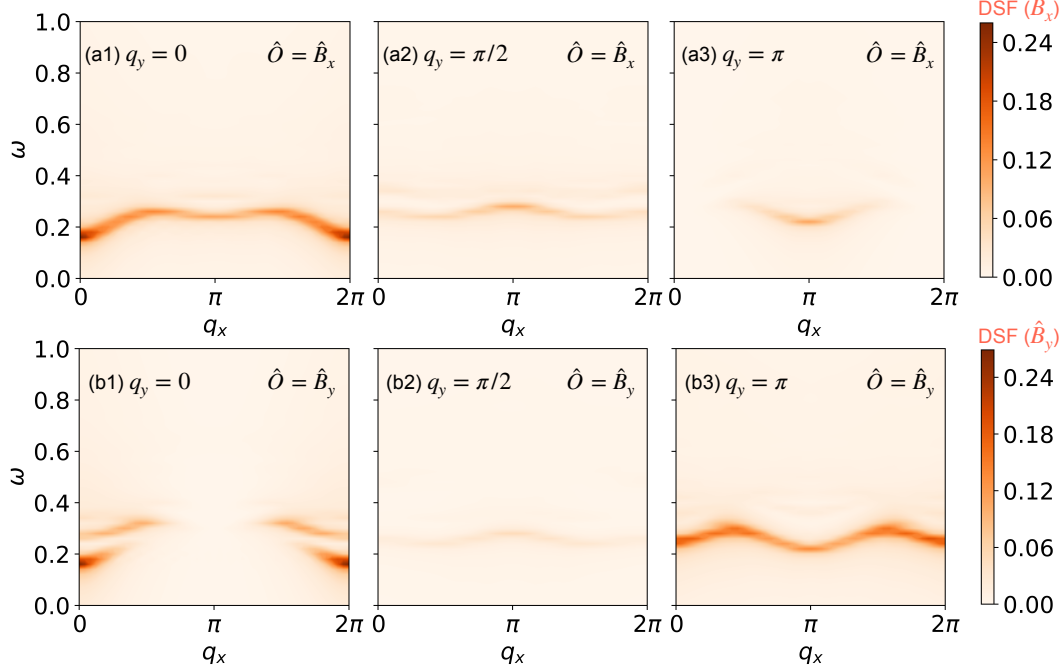


FIG. S6. **Complementary DSFs at $J_2 = 0.6$, $J_\chi = 0.5$.** Here, we show the DSFs of the bond operators \hat{B}_x and \hat{B}_y , respectively.

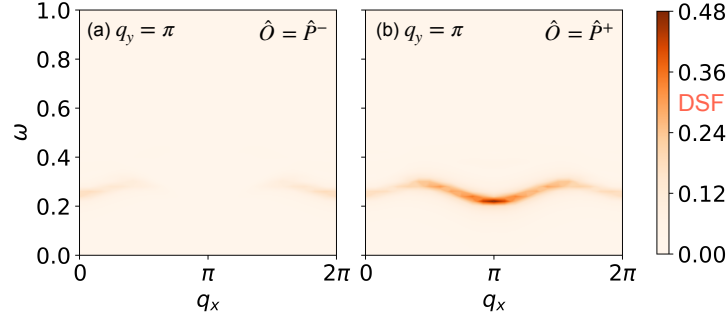


FIG. S7. **Chiral roton mode at $J_2 = 0.6$, $J_\chi = 0.5$.** Here, we show the DSFs in the chiral p-wave channels to demonstrate the low-energy $S = 0$ chiral roton mode at (π, π) .

III. ADDITIONAL INFORMATION OF TDVP SIMULATIONS

To demonstrate the bond dimension up to $\chi = 400$ in the TDVP simulations is well enough for the systems considered in this work, we show the DSFs obtained from different maximum bond dimensions in the \hat{B}_y channel as an example in Fig. S8, and the spectra are well converged.

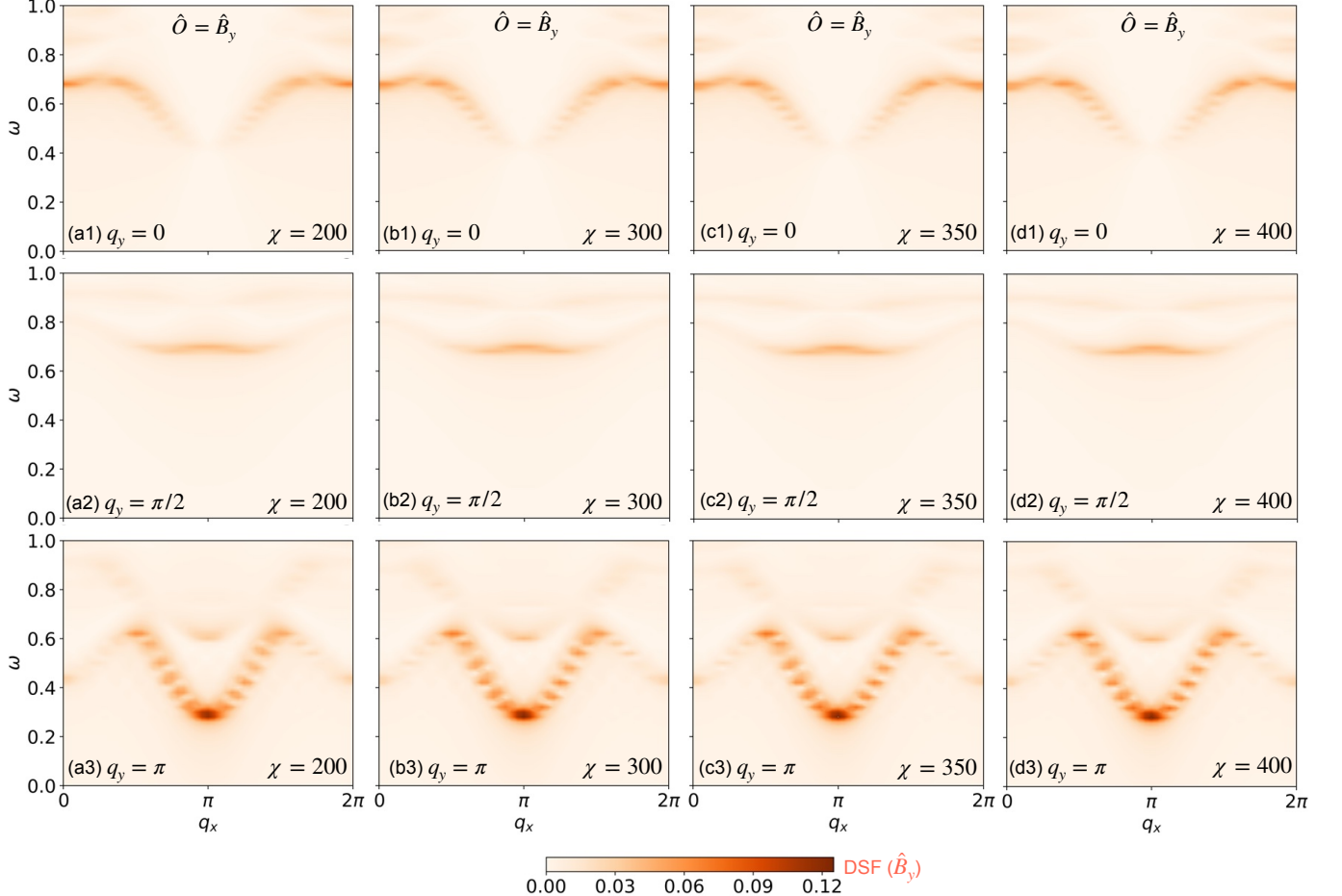


FIG. S8. TDVP results with different bond dimensions. Here, we take the DSFs of the \hat{B}_y operator as an example to illustrate the convergence with respect to the bond dimension. The model parameters are $J_2 = 0$ and $J_\chi = 2$.